Materials Advances

ROYAL SOCIETY OF CHEMISTRY

PAPER

View Article Online
View Journal

Cite this: DOI: 10.1039/d6ma00297h

Valorisation of bourbon distillery waste into single-source hybrid lithium-ion capacitors

Josiel Barrios Cossio,[a] Juan Luis Gómez-Urbano,[b] Sandesh Darlami-Magar,[b] Rodney Andrews,[cd] Ignacio Martin-Gullon,[ef] Andrea Balducci[b] and Marcelo I. Guzman*[ag]

Bourbon, an iconic American whiskey, is primarily produced in Kentucky, which accounts for 95% of the world's supply. Between 2000 and 2024, bourbon output in Kentucky increased sixfold, creating significant sustainability challenges, particularly the disposal of spent grains (stillage), a high-volume byproduct generated at 6–10 times the volume of bourbon produced. This study presents a scalable strategy to upcycle bourbon stillage into high-performance carbon materials for energy storage applications. The process involves different thermal and chemical treatments to obtain both activated and hard carbons. The resulting activated carbons assembled into symmetric electric double-layer capacitors (EDLCs) deliver outstanding electrochemical performance: 96 ± 2% capacitance retention after 10 000 cycles, with energy densities of 23.8–1.9 Wh kg^{-1} and power densities of 0.27–9.2 kW kg^{-1}. Single-source hybrid lithium-ion capacitors (LiCs) assembled with bourbon whiskey-derived hard carbon and activated carbon achieve superior performance, with energy densities of 135–48 Wh kg^{-1} at power densities of 0.215–22 kW kg^{-1}. LiCs also exhibit good galvanostatic retention at 3 A g^{-1}, losing only 17 ± 3% of capacitance and capacity after 5000 charge/discharge cycles and an additional 14 ± 2% after 10 000 cycles. These findings highlight an eco-friendly, circular approach to valorising distillery waste into advanced energy-storage materials, with broad applicability across the spirits and ethanol production sectors.

Received 3rd March 2026,
Accepted 20th April 2026

DOI: 10.1039/d6ma00297h

rsc.li/materials-advances

1. Introduction

Since May 4, 1964, bourbon whisky has been legally recognized as a distinctive product of the United States of America.[1] This spirit is produced domestically from a fermented grain mash containing ≥51% corn, aged in charred new oak barrels at <62.5% v/v, and bottled at ≥40% v/v ethanol.[2] Today, ∼95% of global bourbon production occurs in Kentucky, where this $9 billion industry filled 2.7 million new barrels in 2022.[3] However, for every unit volume of bourbon produced, 6–10 volumes of spent grain (stillage) are generated, creating a major waste management challenge. In Kentucky alone, annual stillage generation exceeds 3.8 × 10^9 L and continues to rise with industry growth.[4]

Traditionally, distillery by-products such as bourbon stillage have been used as livestock feed or soil amendments.[5] Wet stillage is often delivered directly to farms at minimal cost or processed *via* solid–liquid separation and drying to enable transport. Stillage processing and transportation are energy-intensive and costly operations, making them economically prohibitive for small distilleries (≤1.89 × 10^5 L year^{-1}), which account for ∼60% of Kentucky distillation facilities.[6,7] Moreover, stillage production far exceeds regional cattle feed demand, increasing disposal costs and posing operational constraints for many distilleries.[4] Consequently, conventional valorisation routes are increasingly unsustainable both economically and environmentally.

Stillage's high water content (∼90%) further complicates handling, as drying requires substantial energy (2.88 MJ kg^{-1}).[8] Conversely, this property makes stillage an ideal feedstock for hydrothermal carbonization (HTC), which converts wet biomass into carbon-rich hydrochar under subcritical water conditions (<374 °C, <22.064 MPa). HTC typically operates at 180–260 °C and 2–6 MPa for 5–240 min.[9] Hydrochar can serve as a solid fuel, soil amendment, pollutant adsorbent, or

[a] Department of Chemistry, University of Kentucky, Lexington, Kentucky 40506, USA. E-mail: marcelo.guzman@uky.edu
[b] Institute for Technical and Environmental Chemistry, Friedrich Schiller University Jena, and Center for Energy and Environmental Chemistry (CEEC), Jena, Germany
[c] Center for Applied Energy Research, University of Kentucky, Lexington, Kentucky 40506, USA
[d] Department of Chemical and Materials Engineering, University of Kentucky, Kentucky 40506, USA
[e] Chemical Engineering Department, University of Alicante, Spain
[f] Institute of Chemical Process Engineering, University of Alicante, Spain
[g] Lewis Honors College, University of Kentucky, Lexington, Kentucky 40506, USA

precursor for electrochemical materials.[9–11] Additionally, further treatments can be applied to produce suitable hard carbon (HC) and activated carbon (AC) materials featuring increased added value for energy storage applications, such as supercapacitor electrodes.[12,13]

Supercapacitors store energy *via* ion adsorption (electric double-layer capacitors, EDLCs), rapid surface redox reactions (pseudocapacitors), or hybrid mechanisms.[14] They offer high power density, fast charge–discharge rates, and long cycle life, though with lower energy density than batteries.[15] EDLCs typically use high-surface-area carbons such as AC, while hybrid devices combine AC with battery-type electrodes.[16] Symmetric EDLCs employ two AC electrodes in aqueous or organic electrolytes, whereas pairing lithiated HC with AC in Li-based electrolytes yields lithium-ion capacitors (LiCs), bridging the gap between EDLCs and Li-ion batteries.[14,16,17] LiCs typically display energy densities 3 to 5 times greater than that of EDLCs (5–10 Wh kg^{-1}), while retaining 10 times the power density and exceeding the cycle life of lithium-ion batteries (less than 1 kW kg^{-1} and usually 4000 cycles).[18]

Here, we demonstrate the valorisation of bourbon stillage into HC and AC for fabricating single-source symmetric EDLCs and dual-carbon LiCs, a novel application for this biomass waste. The process involves HTC of bourbon stillage to produce hydrochar, followed by high-temperature carbonization under N_2 flow and chemical activation with KOH to obtain HC and AC materials. We systematically characterize the structural and electrochemical properties of these materials and evaluate device performance using commercial electrolytes. This work introduces a scalable, eco-friendly strategy to repurpose distillery waste into advanced energy-storage materials, thereby promoting a circular economy and yielding a value-added product with potential applicability across other spirits and ethanol production sectors.

2. Experimental

2.1. Synthesis of materials

Bourbon stillage was sourced from Wilderness Trail Distillery (Danville, Kentucky) and stored in high-density polyethylene (HDPE) wide-mouth 1 L jars. Immediately after collection, the sample underwent hydrothermal carbonization (HTC) at 200 °C for 45 min under constant pressure and stirring in a 10 L Parr Instrument stirred reactor (model 4556), filled to 50% capacity. The resulting hydrochar served as the precursor for the synthesis of HC and AC.

For the synthesis of HC, hydrochar was carbonized at 1000 °C for 3 h under a nitrogen flow of 110 L h^{-1}, with a heating rate of 500 °C h^{-1}, in a tubular reactor (Thermconcept ROT 60/300/12). The carbonized material was ground in an agate mortar, followed by ball milling in a planetary mill (Fritsch Pulverisette 7) for 2 h at 800 rpm. Milling was performed in four 30 minute cycles with 5 minute rests, maintaining an HC : ball mass ratio of 1 : 6.

In the production of the activated carbons, hydrochar was first carbonized at 500 °C for 2 h under a nitrogen flow of 110 L h^{-1} and a ramp rate of 300 °C h^{-1}. Then, the carbonized hydrochar was ground together with potassium hydroxide (KOH, Carl Roth GmbH, 90.0%) in an agate mortar using a hydrochar : KOH mass ratio of 1 : 4. Lastly, the hydrochar/KOH was heated at 800 °C for two hours under a nitrogen flow of 110 L h^{-1} and a ramp rate of 300 °C h^{-1}. The pre-carbonization step at 500 °C and the activation at 800 °C were both conducted in the same tubular reactor described for HC synthesis. The resulting AC was neutralized with a 0.1 M HCl (Sigma-Aldrich, 37.6%) solution and washed at least four times with hot deionized water (18.2 MΩ cm, ELGA, Purelab Flex 2). Finally, the AC was vacuum-dried (7×10^{-1} bar) at 85 °C in a Buchi glass oven (B-585) overnight.

Synthesis yields for hydrochar, HC, and AC were calculated as:

$$\text{Yield } (\%) = \frac{M_2}{M_1} \times 100\% \quad (1)$$

where M_2 and M_1 represent the dry weights of product and precursor, respectively. Moisture content was determined by weight loss after vacuum drying at 110 °C to constant mass. pH measurements were performed using a calibrated Thermo Scientific Orion Star A221 pH meter after overnight equilibration of 0.4 g of sample in 20 mL of distilled water.[19] More synthesis details are available in Section S1, supplementary information (SI).

2.2. Structural characterization

Raman spectra were recorded using a Thermo Scientific DXR Smart Raman equipped with a 532 nm DPSS laser (9 mW) and a 180° sampling accessory. Each spectrum comprised 120 scans, which were analysed with Omnic 8.2 software using Gaussian/Lorentzian fitting (details in Section S2 and Tables S1–S3 of the SI).

Nitrogen and carbon dioxide adsorption–desorption isotherms at 77 K and 273 K, respectively, were measured on a Micromeritics 3Flex analyser. The Brunauer–Emmett–Teller (BET) surface area was calculated for N_2(g) over the P/P_0 range of 0.05–0.35. The pore size distribution is reported based on both N_2 and CO_2 adsorption isotherms (see Fig. S3 and Section S5 of the SI for details). X-ray diffraction (XRD) patterns were obtained using a Bruker AXS D8 Discover diffractometer (CuK_α radiation, 2θ = 2°–100°, step size 0.02°; details in Section S3, SI). Morphology and elemental composition were examined *via* FEI Quanta 250 FEG Environmental scanning electron microscopy (SEM) equipped with SE/BSE detectors and an Oxford Instruments X-Max 50 mm^2 energy-dispersive X-ray spectroscopy (EDX) sensor at 5–10 kV and magnifications of 500×–1000×.

2.3. Electrochemical characterization

HC electrodes were prepared from aqueous slurries containing 90 wt% HC, 5 wt% Super C65 conductive carbon, and 5 wt% sodium carboxymethyl cellulose binder. Slurries were

homogenized for 20 min at 45 Hz in a Mini-Mill Pulverisette 23, then cast onto copper foil (wet thickness: 50 or 100 μm). After overnight ambient drying, 12 mm discs were punched out from the cast. The resulting electrodes were subsequently vacuum-dried at 85 °C for 24 h, and active mass loadings were 1.13 ± 0.03 mg cm^{-2} for the 50 μm cast and 1.90 ± 0.07 mg cm^{-2} for the 100 μm one. Electrodes were vacuum-dried at 85 °C for another 24 h and transferred to an argon-filled glovebox.

AC electrodes were fabricated analogously, using aluminium foil etched in 5 wt% KOH at 60 °C for 1 min before AC coating. Films with wet thicknesses of 100 and 150 μm yielded active mass loadings of 1.36 ± 0.03 and 1.81 ± 0.08 mg cm^{-2}, respectively, after 12 mm of hole punching and vacuum drying. Electrodes were vacuum-dried as previously described for HC electrodes and subsequently stored under argon.

2.4. Devices manufacturing and testing

HC performance was evaluated in three-electrode Swagelok cells with lithium metal as the counter/reference electrode and LP30 electrolyte (1 M $LiPF_6$ in a 1 : 1 v/v mixture of ethylene carbonate (EC) and dimethyl carbonate (DMC)) containing 2 wt% vinylene carbonate (VC). Galvanostatic cycling was conducted at 0.05–5C between 0.002 and 2.0 V *vs.* Li^+/Li (1C = 372 mAh g^{-1}, the graphite theoretical maximum capacity for lithium intercalation). Symmetric EDLCs were assembled with two AC electrodes separated by a glass microfiber filter (Whatman) soaked in 1 M Et_4NBF_4 in acetonitrile (Skeleton Technologies) inside Swagelok cells. AC electrodes were also independently evaluated in three-electrode Swagelok cells with lithium metal as the reference electrode and conductive carbon as the counter electrode in LP30-2VC. Cyclic voltammetry at 5–50 mV s^{-1} scan rates and galvanostatic cycling at 0.25–20 A g^{-1} for both EDLC and AC electrodes.

LiCs were constructed by pairing pre-lithiated HC (negative electrode) with pre-cycled AC (positive electrode) in a three-electrode Swagelok cell using metallic lithium as reference. Pre-lithiation involved cycling HC in a half-cell against lithium between 0.005 and 2.0 V *vs.* Li^+/Li at 0.05–0.1C, followed by a slow discharge at 0.025C (Scheme S3, SI). AC was pre-cycled in a half-cell against lithium between 2.0 and 4.2 V *vs.* Li^+/Li in LP30-2VC. HC and AC electrodes were recovered by disassembling the cells and pairing them in the LiCs at HC : AC mass ratios of 1.0–1.5. LiCs were cycled between 2.0 and 4.2 V *vs.* Li^+/Li at current densities of 0.05–30 A g^{-1}. Electrochemical tests, including galvanostatic charge–discharge, cyclic voltammetry (CV), and electrochemical impedance spectroscopy (EIS), were performed on a BioLogic VMP-3 potentiostat. Specific capacity, specific capacitance, and current density of electrodes were normalized to the total electrode mass (90 wt% hard carbon or activated carbon, 5 wt% sodium carboxymethyl cellulose, and 5 wt% conductive carbon). Specific capacity, specific capacitance, current density, energy density, and power density of devices were normalized to the total mass of combined electrodes.

3. Results and discussion

3.1. Synthesis of materials

The synthesis of HC and AC began with the HTC of the bourbon whiskey stillage, which was conducted immediately upon arrival at the laboratory from the distillery. The collected stillage was a yellow, acidic dispersion (pH = 3.79 ± 0.03) with 89.95 ± 0.03% water content. HTC yielded 42.8 ± 0.3% hydrochar, a yield comparable to previous reported hydrochar obtained from bio-derived materials under similar hydrothermal conditions.[9,20,21] A proposed HTC pathway is shown in Scheme S1 (SI).

The as-obtained hydrochar showed an amorphous structure (Fig. S1A, SI) with abundant functional groups (Fig. S1B–D, SI). It also displayed a non-porous or macro-porous structure (Fig. S1E), with a low surface area (42.7 ± 0.2 m^2 g^{-1}). Its elemental composition was mainly carbon (61.7 ± 0.3%) and oxygen (25.0 ± 0.1%), with minor hydrogen, nitrogen, aluminium, and silicon (Fig. S1D and F, SI). SEM revealed heterogeneous agglomerates with microcavities and microspheres (Fig. S1G, SI). The acidic pH (4.12 ± 0.02) also indicated abundant acidic functional groups. To enable its use in energy storage devices, hydrochar was converted into HC and AC for capacitor electrodes.

Pyrolysis of hydrochar at 1000 °C produced HC with a yield of 28.05 ± 0.04%. Activation involved carbonizing hydrochar at 500 °C (yield: 34.5 ± 0.3%), followed by KOH activation (1 : 4 hydrochar : KOH) at 800 °C, yielding AC at 51.6 ± 0.1% and a final total yield of 17.4 ± 0.1%. Direct activation without pre-carbonization at 500 °C yielded only 6.7 ± 0.3% of a carbon material (Scheme S2, SI) that also exhibited inferior electrochemical performance (Fig. S2, SI).

3.2. Hard carbon characterization

The physicochemical properties of HCs govern their lithium-ion storage mechanisms, which ultimately constrain the power performance of LiC. Acting as a battery-like electrode, HC enhances LiC energy density through lithium intercalation within layered structures and adsorption in internal pores and defects.[16] However, these storage mechanisms lead to more pronounced capacity fading at high current densities compared to AC-based electrodes.[22,23] Therefore, a deep understanding of HC's physicochemical characteristics is essential for improving high-rate performance without compromising cycling life.

Raman, XRD, and SEM (Fig. 1A–H) confirm the formation of an amorphous, highly disordered, turbostratic, biomass-derived HC. The HC experimental Raman spectrum is fitted to the sum of four first-order (D, G + D′, A, and transpolyacetylene (TPA)) and three second-order (2D, G + D, and $2D_2$) bands (Fig. 1A). The position, intensity, width, and assignment of the identified Raman bands are detailed in Table S1 of the SI. Overall, the D (1338.9 cm^{-1}) and G + D′ (1602.3 cm^{-1}) bands dominate the HC Raman spectrum in terms of intensity. The D (disordered) band is activated by defects, edges, and small sp^2 carbon crystal fragments.[24,25] The G band corresponds to the E_{2g} vibrational mode of sp^2-bonded carbon atoms in graphitic domains.[24,26] Typically observed between 1520 and 1620 cm^{-1},

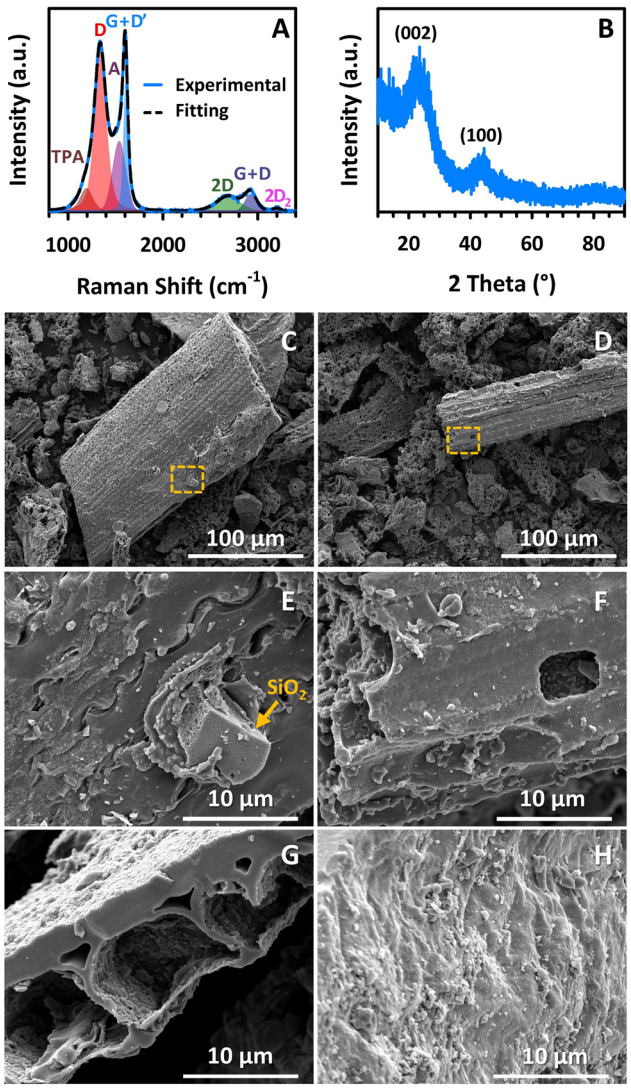

Fig. 1 Physicochemical characterization of hard carbon (HC). (A) Raman spectrum of HC with fitted Gaussian/Lorentzian components (TPA, D, A, G + D′, 2D, G + D, and $2D_2$ in increasing Raman shift), confirming its amorphous structure. (B) X-ray diffraction (XRD) pattern showing peaks at 23.7° and 43.8°, corresponding to the (002) and (100) planes, indicative of distorted graphitic layers mixed with amorphous regions. (C) and (D) Scanning electron microscopy (SEM) images displaying the main surface features, including rod-like structures, numerous cavities, and open channels with a scale bar of 100 µm. (E) and (F) SEM with 10 µm length markers detailing the yellow-highlighted areas in C and D, respectively, which show (E) SiO_2 inclusions and (F) open channels. (G) Lateral and (H) superficial views of fibrous structures using 10 µm micron bars.

its position, intensity, and width correlate with the degree of graphitization.[27] Here, the G band appears at a high shift (1602.3 cm^{-1}) with lower relative intensity (I_D/I_G = 0.93) and a broad width nearly four times that of pristine graphite (~15 cm^{-1}), indicating substantial defects, turbostratic disorder, and low graphitization.[27–29] As HC is a very defective carbon, the D′ (or D_2) band, linked to defects within the graphitic planes, overlaps with the G-band into a broader single peak.[30]

Fitting only the D and G Raman bands within the fingerprint region (400–1800 cm^{-1}) is challenging, indicating the presence of additional signals. Although spectral fitting is not unique, two extra bands (A and TPA) are commonly introduced to achieve a better fit, as detailed in Table S1 (SI).[29–31] The A band, also referred to as the D_3 band, appears around 1536.5 cm^{-1} between the D and G bands and originates from the amorphous carbon fraction caused by point vacancy defects in the HC structure.[30,32] The high synthesis temperature (1000 °C) likely promotes the removal of heteroatoms, leaving these vacancies behind. The A band exhibits a purely Gaussian profile (Table S1, SI), reflecting the statistical distribution of local environments and structural configurations around carbon atoms due to point defects.[30,31] In addition, the TPA band, sometimes denoted D_4, emerges near 1191.0 cm^{-1} and is associated with ordered, conjugated TPA chains (zigzag edge structures) within the HC material.[32,33] The coexistence of D and A bands in the Raman fingerprint region reinforces the amorphous nature of HC and highlights the degree of local disorder.

The ratios obtained by analysing the integrated band area of the first-order Raman spectrum in Fig. 1A, serve as indicators of distinct structural features (Section S2 and Table S3, SI). The analysis reveals a very low degree of graphitization (γ = 0.16) and a very high concentration of structural defects (δ = 0.84). Additionally, the data indicate a very low abundance of TPA-like structures (ϑ = 0.09), small graphitic crystallite size (γ/δ = 0.19), and the presence of amorphous carbon containing both sp^2- and sp^3-hybridized bonds (α = 0.31). A detailed Raman spectroscopy analysis is provided in Section S2 of the SI.

In the second-order Raman spectrum, which comprises overtones and combinations of graphitic lattice vibration modes, two prominent bands appear at 2688.6 cm^{-1} and 2920.3 cm^{-1}, corresponding to the 2D overtone and the G + D combination, respectively. A weaker band at 3202.1 cm^{-1} is assigned to the $2D_2$ overtone. The presence of the 2D, G + D, and $2D_2$ bands indicates that HC consists of a network of small, highly defective, and randomly oriented graphitic domains.[29,34]

The XRD pattern of bourbon whiskey waste-derived HC (Fig. 1B) exhibits two broad diffraction features centred at 2θ = 23.7° ((002) plane) and 43.8° ((100) plane). Both appear as broad humps rather than sharp peaks, with full width at half maximum (FWHM) values of 7.43° for (002) and 5.47° for (100), indicating poor long-range order, nanometric crystallite size (consistent with the Raman γ/δ ratio), high defect density, and an overall amorphous characteristic.[35] The (002) reflection, nearly Gaussian in shape, corresponds to an average interlayer spacing of 0.375 nm, characteristic of turbostratic disorder and variable layer stacking.[36] This spacing, larger than that of graphite (0.333–0.335 nm), is typical of biomass-derived HC and is expected to facilitate lithium-ion intercalation and insertion between layers.[35,36] The Lorentzian-dominant (100) reflection suggests the presence of ~3 nm sp^2 domains embedded within an amorphous matrix.[37,38] Collectively, the XRD results confirm a turbostratic, few-layer HC structure (~three stacked graphene layers), which is favourable for rapid ion and electron transport in alkali-metal-ion storage applications.[16,39] A detailed analysis of XRD parameters is provided in Section S3 of the SI.

No distinct XRD peaks from inorganic impurities are observed in Fig. 1B, suggesting the absence of crystalline phases that could compromise HC structure and performance. However, EDX analysis reveals ~10 μm silicon oxide (SiO_2) inclusions (Fig. 1C–E and Fig. S3A, SI). The broad (002) hump of HC may obscure weaker quartz or cristobalite peaks near 20–23°, as well as the characteristic quartz peak at 26.7°. Furthermore, if present in trace amounts, crystalline SiO_2 may remain undetected by XRD. Thus, SiO_2 is likely present at a low concentration (~1 wt% at the surface, per EDX) or exists as amorphous silica, as the sharp 26.7° α-quartz peak is not clearly discernible.[40] The SEM images in Fig. 1C–H reveal a heterogeneous, hierarchical morphology (Fig. 1C), characterized by large tubular or rod-like fragments (50–200 μm) interspersed with cavities (Fig. 1D, F and G), aligned channels (Fig. 1G), and finer particulate debris (Fig. 1H). Similar tubular or rod-like structures with internal cavities and channels have been reported for other plant biomass-derived carbons.[41] The pronounced surface roughness and open cavities on elongated rods are expected to enhance electrolyte wetting, while the aligned channels provide multiple pathways for electrolyte infiltration and transport.[42]

The surface area of HC (91 ± 1 m^2 g^{-1}) is more than twice that of its precursor (42.7 ± 0.2 m^2 g^{-1}) (Fig. S1E and S3B, SI). Nitrogen adsorption at 77 K indicates that gas uptake occurs primarily in micropores (<2 nm). The steep increase in nitrogen uptake within pores of subnanometer size suggests the presence of ultramicropores (<1 nm), which are only partially accessible to N_2, leading to an underestimation of true ultramicroporosity. Micropores and nanopores serve as key sites for lithium pore filling, contributing to plateau capacity, while a moderate surface area supports capacitive ion storage.[16] However, excessively high surface areas (>100 m^2 g^{-1}) can promote solid electrolyte interphase (SEI) formation and cause irreversible capacity loss.[16] To achieve a more accurate and comprehensive pore structure analysis, complementary CO_2 adsorption at 273 K and unified density functional theory pore size distribution (DFT-PSD) calculation for N_2 and CO_2 gases is performed (Fig. S3B, SI). The unified CO_2/N_2 DFT-PSD reveals a predominantly microporous structure for the HC, with the pore volume concentrated in ultramicropores and a minor contribution from mesopores and macropores (Fig. S3B, SI).

Under an air atmosphere, TGA analysis (Fig. S3C, SI) shows an initial 6.45% mass loss below 105 °C, attributed to physisorbed water and volatile species, followed by negligible change up to 524 °C. Beyond this point, rapid oxidative decomposition of the carbon matrix occurs between 524 °C and 701 °C, resulting in an 86.75% mass loss (typical behaviour for disordered carbons). The residual mass at 800 °C is 6.80%, corresponding to inorganic ash content (silicates and metal oxides). Overall, these physicochemical characteristics highlight the development of an environmentally sustainable and cost-effective HC material that combines hierarchical morphology, pore-filling capacity, and structural stability, making it a promising candidate for LiC anodes.

3.2.1. Hard carbon electrochemical evaluation. The electrochemical performance of HC as an LiC anode was first assessed in a half-cell configuration using lithium metal as both counter and reference electrodes (Fig. 2). Fig. 2A shows the rate capability of three bourbon whiskey waste-derived HC electrodes tested at 0.1, 0.2, 0.5, 1.0, 2.0, and 5.0C (where 1C = 372 mAh g^{-1}) in LP30-2VC electrolyte over a potential range of 5 mV to 2 V *vs.* Li^+/Li. Rate capability reflects electrode performance at high current, where increasing the C-rate limits the achievable capacity.[43] The HC electrode delivered an initial discharge capacity of 302 ± 12 mAh g^{-1} at 0.1C. Capacity decreased markedly from 302 mAh g^{-1} at 0.1C to 90 mAh g^{-1} at 5C, retaining 48.8% of its initial capacity at 1C and only 29.8% at 5C. Overall, these values are comparable to those reported for many hard carbon anodes, indicating that the

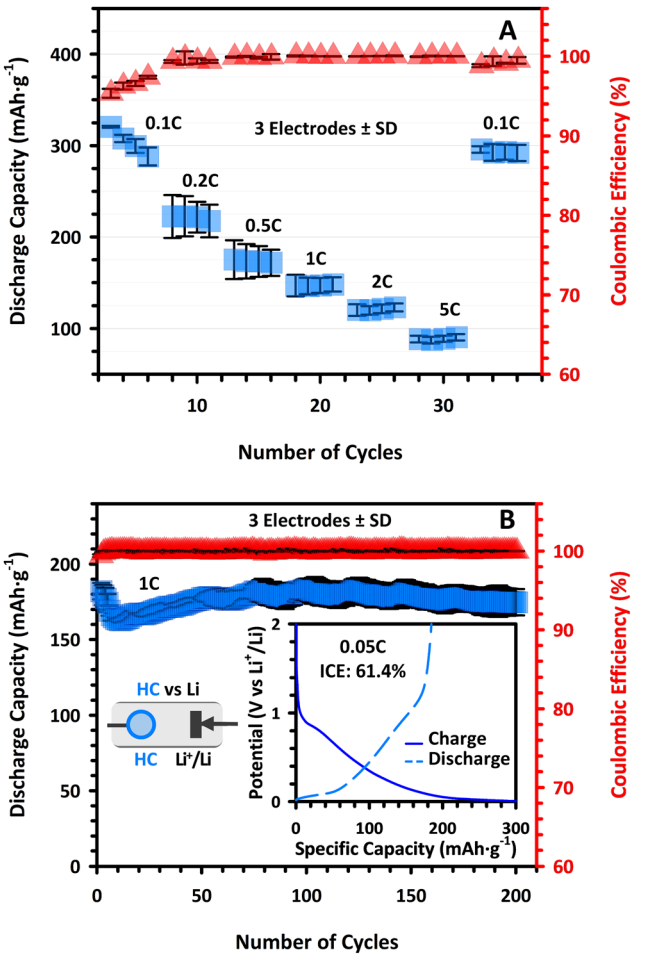

Fig. 2 Electrochemical performance of HC electrodes tested as working electrodes in Swagelok-type half-cells with lithium metal as both the counter and reference electrodes in LP30-2VC electrolyte. (A) Discharge capacity and coulombic efficiency for three independent HC electrodes cycled at C-rates of 0.1, 0.2, 0.5, 1, 2, and 5 (1C = 372 mAh g^{-1}). (B) Long-term cycling stability at 1C over 200 cycles. Left inset: Schematic of the half-cell configuration. Right inset: First-cycle charge–discharge profile at 0.05C, highlighting an initial coulombic efficiency (ICE) of 61.4%. Error bars represent the standard deviation of discharge capacity across the three electrodes.

material already exhibits a satisfactory rate capability under the present conditions.[17,18,22] Although dedicated optimization was not performed (*e.g.*, pyrolysis temperature, particle size) to enhance high-rate performance, the observed results evince significant potential for further improvement without diminishing the material's existing advantageous properties.

HC also demonstrates excellent structural stability and capacity recovery. When the current was reduced back to 0.1C, the specific capacity returned to 292 ± 1 mAh g^{-1}, recovering 96.9% of its initial value. This remarkable recovery confirms that the capacity loss at high rates is primarily due to kinetic limitations rather than irreversible material degradation, indicating strong structural integrity. Furthermore, the low standard deviations (±1–2 mAh g^{-1}) across all subsequent measurements (from 0.2C through the return to 0.1C) validate consistent performance among the three tested electrodes.

The initial galvanostatic charge–discharge profile at 0.05C (Fig. 2B, right inset) exhibited a first charge capacity of 601 mAh g^{-1} and a corresponding discharge capacity of 369 mAh g^{-1}, yielding an initial coulombic efficiency (ICE) of 61.4 ± 0.3%. The significant irreversible capacity is associated with SEI formation, which stabilizes within the first few cycles at 0.1C. The high capacity observed in the initial cycles can be attributed to the HC average d_{002} spacing of 0.375 nm, which exceeds the graphite range (0.333–0.335 nm), allowing large amounts of Li^+ to access interlayer sites through intercalation (plateau region) and surface adsorption (slope region) (Fig. 2B, inset and Fig. S4, SI). In addition, sp^3- and TPA-structures should provide additional structural defects for surface Li^+ adsorption. A detailed analysis of Li-ion storage mechanisms and SEI development is provided in Fig. S4, SI. To further assess HC stability, long-term cycling was conducted over 200 cycles at 1C in the same two-electrode cell configuration (Fig. 2B, left inset). Fig. 2B shows an average discharge capacity of 177 ± 5 mAh g^{-1} for three electrodes over 200 cycles, with nearly 100% coulombic efficiency throughout most cycles and 96.2% capacity retention. These results demonstrate exceptional long-term cycling stability and electrochemical activation behaviour. During extended cycling at 1C, the specific capacity increased from 170 ± 5 mAh g^{-1} during the first 50 cycles to a stable 179 ± 2 mAh g^{-1} for the remaining 150 cycles. This gradual increase is attributed to the progressive wetting of HC's microporous structure, which improves lithium access to previously inaccessible active sites. The combination of high specific capacity, strong performance at elevated C-rates, and excellent capacity retention indicates favourable kinetics and the formation of a stable SEI, making this material a suitable candidate for pairing with an AC cathode in a hybrid energy storage device. To ensure complete SEI formation, a prelithiation strategy was employed before LiC assembly (Scheme S3, SI).

3.3. Activated carbon characterization

While HC delivers high energy density for the hybrid device, AC provides high power capability and rapid charge/discharge by storing energy through lithium adsorption at the electric double layer (EDL). The performance of the AC cathode is inherently tied to its structural and textural properties (Fig. 3), which dictate ion adsorption, charge transfer, and long-term stability.[44,45] Fig. 3A shows the experimental Raman spectrum of AC along with a fitted curve representing the sum of deconvoluted bands. Like HC, the AC spectrum is dominated by the D and G + D′ bands (Table S2, SI). Additional Raman

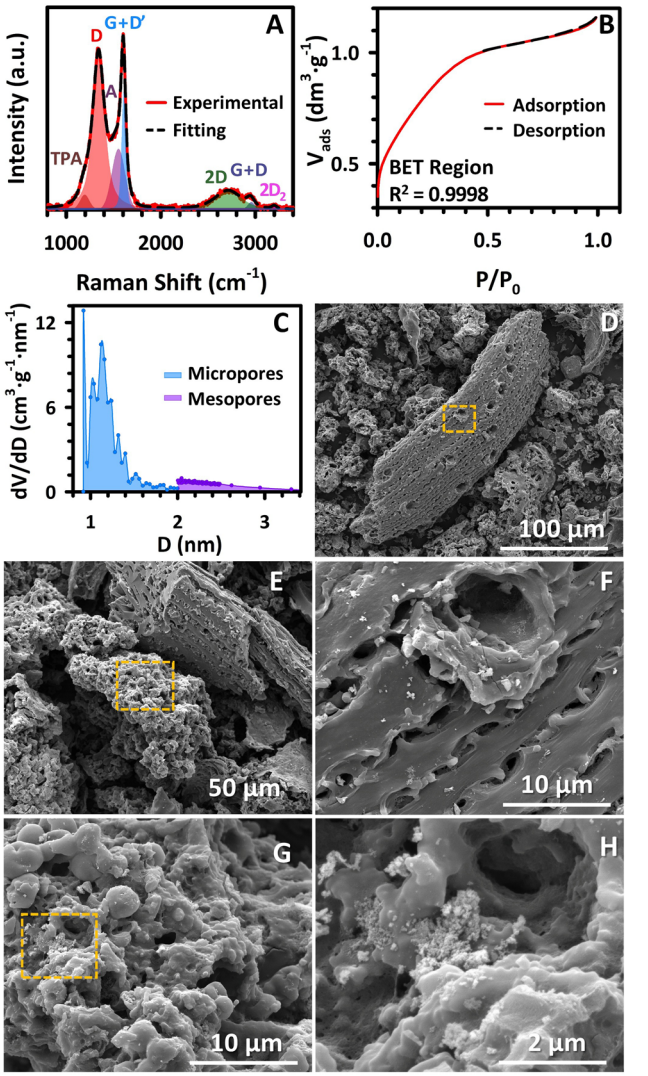

Fig. 3 Physicochemical characterization of AC. (A) Raman spectrum with experimental data and fitted sum of deconvoluted D, G + D′, A, TPA, 2D, G + D, and $2D_2$ bands. (B) N_2 volume adsorbed (V_{ads}) *vs.* relative pressure (P/P_0) with BET fitting in the 0.05–0.35 P/P_0 range, yielding a specific surface area of 2861 ± 4 m^2 g^{-1}. (C) Pore size distribution by the ratio of the first derivative of the volume (d*V*) and the first derivative of the average pore diameter (d*D*) *vs.* the average pore diameter (*D*), showing the abundance of micro- (<2 nm) and small mesopores (2–50 nm). (D)–(H) SEM images that illustrate the abundance of heterogeneous motifs present in AC, with scale bars of (D) 100 µm and (E) 50 µm. (F) Details of open cavities highlighted in yellow in *D* with a calibrated length of 10 µm. (G) Details of the rounded motif highlighted in yellow in (E) with a magnification indicator of 10 µm. (H) Further details of surface cavities and heterostructures highlighted in yellow in (G) with a scale bar of 2 µm, illustrating the dominant surface morphology, heterogeneity, and abundance of variable-sized cavities.

features include secondary defect and amorphous A and TPA bands, as well as 2D, G + D, and $2D_2$ bands in the overtone region (Table S2, SI).

The D band exhibits high intensity (I_D/I_G = 0.89), confirming a significant defect density, while its broad width reflects a wide variety of defect types.[24] This strongly indicates aggressive chemical activation, which introduces vacancies, pores, and numerous new edge planes into the carbon framework.[46] The G band is shifted to a higher wavenumber than in pristine graphite ($\sim$1582 cm^{-1}), suggesting the presence of small, isolated sp^2 graphitic domains embedded in a disordered matrix.[47] Its relatively narrow full width at half maximum (FWHM) implies that these nanocrystallites are fairly uniform despite their disordered surroundings.[27] Nevertheless, the G band dominates the spectrum around 1580–1620 cm^{-1}, making the D′ (or D_2) band, which has low intensity, visually blend with it. The D_2 band is attributed to disorder or defects at the edges of graphitic crystallites.[30] The amorphous A band, with notable intensity and a pure Gaussian profile, points to a substantial fraction of amorphous carbon.[30,32] KOH activation reduces the size of graphitic crystallites into smaller, more defective nanocrystals, reorganizing the AC structure into a highly disordered and amorphous structure. Additionally, the TPA band, associated with zigzag edges, indicates the formation of sp^3-hybridized sites within the carbon network.[32]

The 2D band, with its broad FWHM, reflects the highly disordered nature of AC, indicating the absence of regular stacking among any graphitic layers that may be present (Table S2, SI).[27] The G + D band further confirms structural disorder, as its activation requires the presence of defects.[48] The weak $2D_2$ feature reinforces this defect-rich framework. Overall, Raman analysis (Fig. 3A) demonstrates that AC exhibits a highly disordered, porous, and defect-dense structure, characteristics that typically translate into an exceptionally large surface area, essential for high-performance capacitive energy storage.

Bourbon-derived HC and AC display comparable Raman features, with nearly identical band positions and equivalent signal assignations (Tables S1 and S2, SI). However, their structural characteristics, as determined from deconvoluted Raman spectra, differ systematically (Table S3, SI). HC shows greater graphitization and crystallite growth, along with a higher abundance of sp^3-hybridized carbon bonds and TPA-like structures, compared to AC. In contrast, AC exhibits a higher defect concentration, along with broader and weaker D- and G-bands, indicating lower crystallinity and uniformity relative to HC.

Nitrogen adsorption at cryogenic temperatures (Fig. 3B) for AC confirms the development of an exceptionally high surface area of 2861 $\pm$ 4 $m^2\ g^{-1}$. As noted earlier, AC electrodes store Li-ion by adsorption at the EDL. A large surface area promotes extensive EDL formation, providing more adsorption sites and thereby enhancing specific capacitance and energy density.[48] However, surface area alone is not sufficient; pore size (Fig. 3C and Fig. S5A, B, SI) and connectivity are equally critical for performance, particularly at high power rates.[48,49]

The N_2 adsorption isotherm in Fig. 3B exhibits a steep uptake at $P/P_0 < 0.1$, indicating the presence of abundant micropores (<2 nm), as shown in Fig. 3C. Specifically, a large abundance of ultra-micropores (<0.7 nm) is confirmed by CO_2 adsorption at 273 K (Fig. S5A and B, SI). KOH activation is highly effective in generating micropores, resulting in both high surface area and substantial gas adsorption capacity (N_2 cumulative pore volume: 1.5 $cm^3\ g^{-1}$).[50] The pronounced additional uptake between 0.1 and 0.5 P/P_0 reflects, in addition to the micropores, a large abundance of 2–5 nm mesopores, confirmed by the DFT-PSD in Fig. S5A, SI. In contrast, the lack of a clear hysteresis loop in Fig. 3B indicates that larger mesopores (roughly 5–50 nm) are not abundant, which is also consistent with the limited volume of wider mesopores observed in Fig. S5A, SI. DFT-PSD shows that around 67% of the total gas adsorption occurs in micropores (28% in ultra-micropores), while the remaining 33% occurs in mesopores (31% in pores 2 to 5 nm wide).

Micropores are essential for maximizing surface area and EDL formation,[51,52] while mesopores facilitate rapid ion transport from the bulk electrolyte to micropores, improving power density.[52,53] Macropores act as reservoirs, ensuring electrolyte saturation.[52] The limited development of large mesopores could limit connectivity between surface-accessible voids and the internal micropore-small mesopore network, potentially creating diffusion bottlenecks during high-rate cycling. While macropores facilitate electrolyte infiltration, insufficient distribution of variable-size mesopores could limit ion transport, resulting in performance limitations at high current densities.

SEM images (Fig. 3D–H) illustrate AC morphology at different magnifications and scale bars of 100 μm, 50 μm, 10 μm, and 2 μm. The AC structure appears amorphous, featuring (Fig. 3D and E) fibrous motifs and (Fig. 3E and G) bulky domains. Both AC and HC display fibrous motifs (Fig. 3D and E) due to the single-source plant-derived biomass waste. However, AC features large surface cavities, where HC exhibits SiO_2 inclusions. Fig. 3D and the details of the yellow-highlighted area in Fig. 3F show these large surface cavities within the fibrous structures. Additionally, large macropores are visible in Fig. 3H. These large surface cavities and macropores act as entry points and reservoirs for the electrolyte.

3.3.1. Activated carbon electrochemical evaluation. The electrochemical performance of bourbon-derived ACs was first assessed in symmetrical EDLCs (Fig. S6, SI). Cyclic voltammetry (Fig. S6A, SI) at scan rates from 5 to 50 mV s^{-1} shows nearly rectangular profiles. The rectangular voltammogram profiles are retained as the scan rate increases from 5 to 50 mV s^{-1}, indicating good capability to operate at high rates. In good agreement, galvanostatic charge–discharge measurements (Fig. S6B, SI) reveal a capacitance retention of 92% from 0.1 A g^{-1} (27.4 $\pm$ 0.8 F g^{-1}) to 1.0 A g^{-1} (25.1 $\pm$ 0.3 F g^{-1}). At higher currents, capacitance gradually declines from 24.2 $\pm$ 0.5 F g^{-1} at 2.0 A g^{-1} to 17 $\pm$ 2 F g^{-1} at 10 A g^{-1}, retaining over 60% of the initial value.

Stability was assessed *via* a float test at 2.7 V with intermittent cycling at 1 A g^{-1} every 10 hours (Fig. S6C, SI). EDLCs

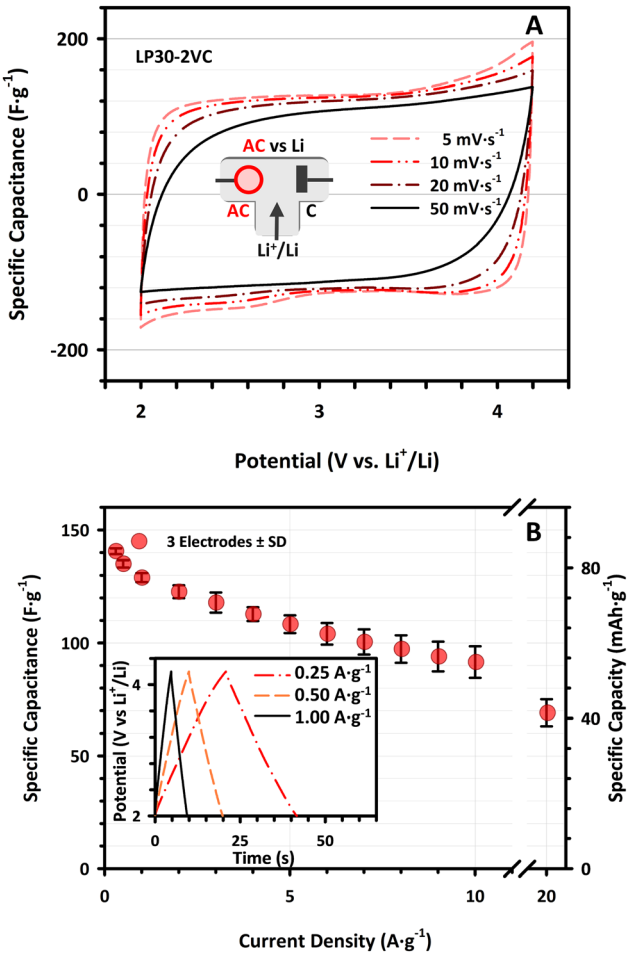

Fig. 4 Electrochemical performance of AC electrodes in a three-electrode configuration using Li^+/Li as the reference and carbon as the counter electrode in the LP30-2VC electrolyte. (A) Cyclic voltammograms at scan rates of 5–50 mV s^{-1}; the inset shows the three-electrode schematic. (B) Galvanostatic charge–discharge curves at current densities from 0.25 to 20 A g^{-1}; the inset highlights profiles at 0.25, 0.50, and 1.0 A g^{-1}. Error bars represent the standard deviation of specific capacitance across three replicates.

retained 90% of their initial capacitance after 100 h and 88% after 200 h. Long-term cycling (Fig. S6D, SI) over 15 000 cycles at 1 A g^{-1} resulted in only 4% loss after 10 000 cycles and an additional 6% over the final 5000 cycles. Both tests indicate excellent durability and low fade rates, underscoring AC's potential for practical energy storage.

Fig. 4A shows the cyclic voltammetry of AC in a half-cell configuration using LP30-2VC electrolyte within a 2.0–4.2 V window *vs.* Li^+/Li. These potential limits were chosen to mimic the performance of the AC when operating as the positive electrode in the LiC. The voltammograms exhibit a nearly rectangular shape across scan rates from 5 to 50 mV s^{-1}, indicating ideal capacitive behaviour with negligible faradaic contributions. Galvanostatic charge–discharge curves (Fig. 4B, inset) display the characteristic triangular profile with minimal ohmic drop and no faradaic processes. Fig. 4B shows a gradual decline in capacitance from 141 ± 1 F g^{-1} at 0.3 A g^{-1} to 92 ± 7 F g^{-1} at 10 A g^{-1}, retaining over 65% of its initial value. Overall, AC in LP30-2VC delivers a high specific capacitance of 129 ± 2 F g^{-1} at 1.0 A g^{-1} and maintains 71% retention at 10 A g^{-1} (92 ± 7 F g^{-1}). This robust capacitive behaviour confirms efficient double-layer formation and excellent rate capability, guiding the optimization of AC mass loading for LiC assembly (Fig. S7, SI).

3.4. Lithium-ion capacitor performance

Fig. S7, SI, shows that the specific capacities of HC and AC electrodes in half-cells are significantly different. HC-based electrodes exhibit capacities more than 3 times higher than AC at low current densities. However, when current densities increase, the capacities of HC and AC approach each other, with a ratio of 1.2 : 1 at 2 A g^{-1}. Consequently, the LiC performance is experimentally evaluated using HC : AC mass ratios ranging from 1 : 1 to 1.5 : 1 (Fig. S8, SI). These configurations intentionally oversize the negative electrode to prevent full capacity utilization and minimize the risk of lithium plating. Balanced HC/AC ratios are also critical for optimizing energy, power, and stability in LiCs.[45] Fig. S8, SI confirms that a 1 : 1 ratio delivers superior energy and power densities compared to LiC configurations with higher HC/AC mass ratios. This ratio was used consistently across all tests shown in Fig. 5A–C.

LiC devices were assembled using prelithiated HC and precycled AC electrodes in LP30-2VC electrolyte. Fig. 5 presents the electrochemical performance of LiCs with optimized mass loading. One major cause of capacity fade in LiCs is lithium plating, the unwanted deposition of metallic lithium on the HC surface when its potential (E_{HC}) falls at or below 0 V *vs.* Li^+/Li.[54] To confirm the absence of lithium plating ($E_{HC} > 0$ V *vs.* Li^+/Li), a Li^+/Li reference electrode was included during testing at various current densities as a third electrode (Fig. 5A, right inset). This configuration also enabled monitoring of the AC electrode potential alongside the device voltage (Fig. 5A, left inset).

The left inset of Fig. 5A shows a complete charge/discharge profile of a model LiC cycled between 2.0 and 4.2 V at 1 A g^{-1}. LiCs were tested from 0.05 to 30 A g^{-1} (Fig. S9 and Table S4, SI), but only 0.05–6 A g^{-1} are shown in Fig. 5A due to the high variability of specific capacitance values (relative standard deviation (RSD) ≥ 21%) obtained beyond 6 A g^{-1}. At 0.05 A g^{-1}, LiCs delivered a specific capacitance of 73.6 ± 0.5 F g^{-1} and a specific capacity of 44.1 ± 0.5 mAh g^{-1} (normalized to the total electrode mass). At 6 A g^{-1}, the devices retained 72% of their initial capacitance (53 ± 1 F g^{-1}) and 52% of their initial capacity (23 ± 1 mAh g^{-1}).

During the float test (Fig. 5B), LiCs retained 80 ± 2% of its initial capacitance and 67 ± 3% of its initial capacity after 200 h at 1 A g^{-1}. This behaviour is consistent with parasitic electrolyte oxidation above 4.0 V, facilitated by the high surface area, oxygen groups, and microporosity of the AC cathode.[55–57] The resulting byproducts may block pores and increase resistance, which mainly manifests as the observed capacitance fade.[56,58] The somewhat larger loss in specific capacity likely arises from

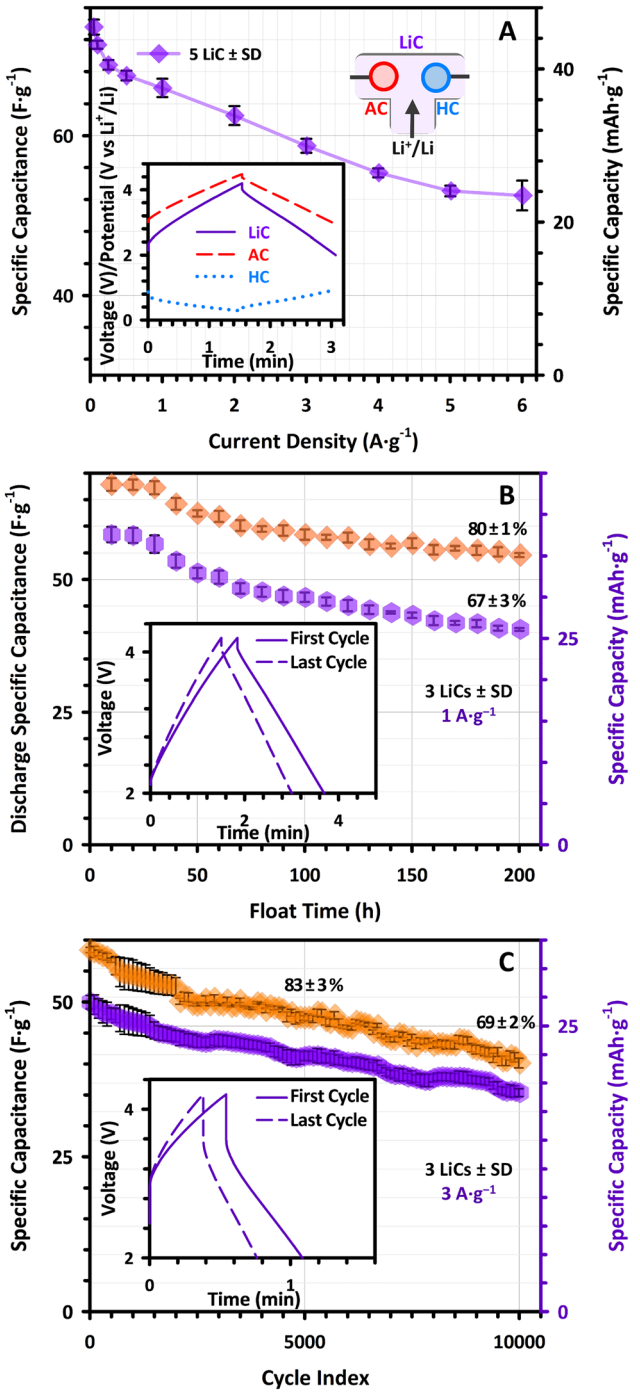

Fig. 5 Electrochemical performance of LiC devices assembled with a precycled AC and a prelithiated HC in a three-electrode Swagelok-type cell. (A) Specific capacitance and capacity retention at 0.05–6 A g^{-1} (error bars: SD from five devices). Left inset: Galvanostatic profiles at 1 A g^{-1} showing LiC voltage (violet) and AC (red) and HC (blue) potentials *vs.* Li^+/Li, with HC remaining above 0 V. Right inset: Schematic of the three-electrode configuration with AC, HC, and the Li reference. (B) Float test of LiC devices at 1 A g^{-1} over 200 h, with capacitance and capacity retentions after 200 h test and an average Coulombic efficiency (CE) of 99.9 ± 0.1%. Inset: Charge/discharge profiles at 10 h and 200 h. (C) Cycling stability of LiC devices at 3 A g^{-1}, showing capacitance and capacity retention after 5000 and 10 000 cycles, CE = 99.93 ± 0.02%. Inset: Profiles at the 10th and 999th cycles.

additional battery-type degradation at the prelithiated HC anode during float, such as SEI growth and loss of cyclable lithium.[59,60] Consequently, a stronger apparent fade in capacity than capacitance is expected, even though the overall capacitive response remains robust. Retaining 80% of the initial capacitance and 67% of the initial capacity after 200 h under a demanding high-voltage float protocol is highly encouraging for unoptimized, additive-free, biomass-waste-derived LiCs.

LiCs also exhibited good retention when galvanostatically cycled for 10 000 cycles at 3 A g^{-1} (Fig. 5C), with only 17 ± 3% capacitance and capacity loss after 5000 cycles and an additional 14 ± 2% after 10 000 cycles. The retention of 83% of specific capacitance and capacity after 5000 cycles at 3 A g^{-1} suggests that high-current cycling is primarily influenced by reversible resistive and transport changes rather than by distinct battery-type degradation. This behaviour is advantageous for high-power applications.[61,62]

Fig. 6 presents Ragone plots comparing the specific energy and power of the assembled EDLC and LiC devices. EDLCs exhibit energy densities from 23.8 ± 0.7 Wh kg^{-1} at 270 ± 4 W kg^{-1} to 1.9 ± 0.7 Wh kg^{-1} at 9.2 ± 5 kW kg^{-1}. In contrast, LiCs deliver 135 ± 3 Wh kg^{-1} at 215 ± 5 W kg^{-1}, decreasing to 48 ± 2 Wh kg^{-1} at 22 ± 1 kW kg^{-1}. While both systems achieve comparable high-power performance, LiCs provide substantially higher gravimetric energy densities, ranging from 5 to 25 times those of EDLCs across 0.05–6 A g^{-1}. This combination of exceptional energy and power density highlights the effectiveness of the LiC hybrid configuration. The superior performance of LiCs stems from selecting a single, suitable source of biomass waste (bourbon stillage) that pairs a high-power, ion-adsorptive AC electrode with a high-capacity HC electrode. Prelithiation of HC is a critical step because it minimizes irreversible lithium loss, lowers the HC operating potential, and widens the LiC

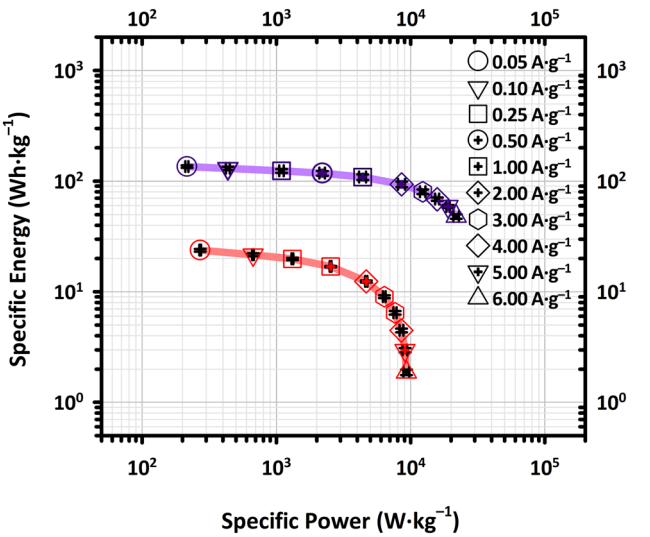

Fig. 6 Ragone plots comparing the electrochemical performance of the assembled LiC and EDLC devices. Gravimetric specific energy and power densities are shown with error bars representing the standard deviation from independent measurements of each device. Specific energy and power densities are normalized to the total mass of combined electrodes.

voltage window. A larger voltage directly translates into higher energy density while preserving high power, enabled by the rapid ion kinetics of the AC electrode. When benchmarked against recent reports using undoped biomass-derived carbons, these results are highly competitive.[17,18,22]

3.5. The fitness of bourbon distillery waste valorisation for LiCs

Bourbon stillage is distinguished among lignocellulosic distillery wastes by its elevated protein (26 ± 2%) and fat (9 ± 2%) contents.[4] Its high-water proportion (89.95 ± 0.03%) and inherent acidity (pH = 3.79 ± 0.03) make HTC (200 °C, 45 min) an effective single-step process for producing hydrochar with exceptionally low mineral content (1.58 ± 0.02%). This process induces intrinsic cross-linking defects (which enforce HC lattice turbostratic disorder) and extrinsic heteroatom functional groups (25.0 ± 0.1% O and 4.7 ± 0.2% N), both of which impact the resulting structures and Li^+ storage capacity of HC and AC. Another distinct class of intrinsic defects, sp^3-hybridized cross-linking carbon bonds and TPA chains at grain boundaries, has been confirmed by Raman spectroscopy in both HC and AC. To our knowledge, these structures have not been reported for purely lignocellulosic or purely protein-rich derived carbons.

The symmetric EDLCs assembled deliver 23.8 ± 0.7 Wh kg^{-1} with 96% capacitance retention after 10 000 cycles in 1 M Et_4NBF_4 in ACN. This high cycling stability ranks among the best reported for any distillery- or fermentation-waste-derived activated carbon in an organic electrolyte (Table S5, SI). The resulting dual-carbon, single-source LiC achieves 135 ± 3 Wh kg^{-1} at 215 ± 5 W kg^{-1} and 48 ± 2 Wh kg^{-1} at 22 ± 1 kW kg^{-1} with 69% capacity retention after 10 000 cycles, outperforming the closest published biomass single-source analog (*Pinus radiata*, 111 Wh kg^{-1}, 60% at 10 000 cycles) without any external dopant, template, or pretreatment (Table S6, SI). Taken together, these results demonstrate that bourbon stillage is not merely a waste stream amenable to valorisation, but a chemically self-consistent precursor whose accidental biochemical composition generates a dual-defect carbon architecture that rivals purpose-engineering systems.

4. Conclusions

Bourbon whiskey stillage was successfully upcycled into high-value carbonaceous materials, hydrochar, HC, and AC. HTC at 200 °C for 45 min provided a cost-effective and environmentally sustainable route to convert stillage into hydrochar. Subsequent carbonization under nitrogen at 1000 °C produced HC, while chemical activation with KOH (1 : 4 ratio) at 800 °C yielded AC. Both HC and AC served as active materials for high-performance single-source electrochemical capacitors. Symmetric AC-fabricated EDLCs exhibited exceptional cycling stability, retaining 96% of their initial gravimetric capacitance after 10 000 charge/discharge cycles. Their performances are highly competitive, delivering specific energy and power densities of 23.8–1.9 Wh kg^{-1} at 0.27–9.2 kW kg^{-1}. Furthermore, hybrid lithium-ion capacitors achieved superior energy densities of 135–48 Wh kg^{-1} at power densities of 0.215–22 kW kg^{-1}. These results establish a green chemistry framework for transforming bourbon whiskey waste into single-source electrode materials for high-performance supercapacitors, with potential for scalability to other spirits and ethanol-producing industries.

Author contributions

Conceptualization, writing – reviewing, and editing original draft, formal analysis, data curation, and visualization: J. B. C., J. L. G.-U., A. B., and M. I. G.; methodology and investigation: J. B. C., J. L. G.-U., S. D. M., and I. M.-G.; resources, supervision, funding acquisition, and project administration: M. I. G. and A. B. All authors (J. B. C., J. L. G.-U., S. D. M., R. A., I. M.-G., A. B., and M. I. G.) have read and agreed to the final version of the manuscript.

Conflicts of interest

The authors declare no competing financial interests. The funders had no role in the design of the study, or interpretation of data, in the writing of the manuscript, or in the decision to publish this material.

Data availability

All data supporting this article are provided in the document and in part in the supplementary information (SI). Supplementary information: additional discussion, Schemes S1–S3, Fig. S1–S9 and Tables S1–S6. See DOI: https://doi.org/10.1039/d6ma00297h.

Acknowledgements

The authors acknowledge financial support from the U.S. National Science Foundation (NSF) under award number 2403875 (M. I. G.). J. B. C. gratefully acknowledges support from a University of Kentucky NSF Research Traineeship Fellowship (UK NRT) funded by NSF under award number 1922694. This publication was supported by the University of Kentucky Materials Science Research Priority Area. J. L. G.-U. acknowledges the German Chemical Industry Fund for financial support through the Liebig Fellowship. S. D. M and A. B. acknowledge the financial support from Deutsche Forschungsgemeinschaft (DFG) for projects BA4956/21-1. The authors thank Dr Eduardo Santillan-Jimenez for access to CAER facilities and support under UKNRT. We also thank Dr Jason Backus (Kentucky Geological Survey) for assistance with XRD measurements, Dr Michela Martinelli for N_2 and CO_2 physisorption support at CAER, and Dr Nicolas Briot for SEM-EDX analysis at the UK Electron Microscopy Center.

References

1 U.S. Congress. S. Con. Res. 57, 88th Congress, 1964.
2 Alcohol and Tobacco Tax Trade Bureau, CFR Title 27, Chapter I, Subchapter A, 2022, 39.
3 P. Coomes and B. Kornstein, *Kentucky Distillers Association*, 2023, p. 91.
4 D. Hockensmith, C. Crofcheck and T. J. Barzee, *J. Environ. Manage.*, 2024, **367**, 121975.
5 K. J. E.-P. Kouame, E. O. Falade, Y. Zhu, Y. Zheng and X. Ye, *Food Chem.*, 2025, 143326.
6 E. C. Umego and C. Barry-Ryan, *Crit. Rev. Food Sci. Nutr.*, 2024, **64**, 8231–8247.
7 J. W. Lehmkuhler and E. S. Vanzant, *Appl. Anim. Sci.*, 2022, **38**, 456–465.
8 J. D. Murphy and N. M. Power, *Fuel*, 2008, **87**, 1799–1806.
9 J. O. Ighalo, F. C. Akaeme, J. Georgin, J. S. de Oliveira and D. S. Franco, *Sustainability*, 2025, **17**, 1660.
10 A. Lorente, J. Remón, M. Salgado, A. J. Huertas-Alonso, P. Sánchez-Verdú, A. Moreno and J. H. Clark, *ACS Sustainable Chem. Eng.*, 2020, **8**, 18982–18991.
11 D. Bona, D. Bertoldi, G. Borgonovo, S. Mazzini, S. Ravasi, S. Silvestri, C. Zaccone, B. Giannetta and F. Tambone, *Waste Manage.*, 2023, **159**, 75–83.
12 M. Prieto, H. Yue, N. Brun, G. J. Ellis, M. Naffakh and P. S. Shuttleworth, *Polymers*, 2024, **16**, 2633.
13 S. Ghosh, R. Santhosh, S. Jeniffer, V. Raghavan, G. Jacob, K. Nanaji, P. Kollu, S. K. Jeong and A. N. Grace, *Sci. Rep.*, 2019, **9**, 1–15.
14 P. Simon and Y. Gogotsi, *Nat. Mater.*, 2008, **7**, 845–854.
15 P. Simon, Y. Gogotsi and B. Dunn, *Science*, 2014, **343**, 1210–1211.
16 S. K. Saju, S. Chattopadhyay, J. Xu, S. Alhashim, A. Pramanik and P. M. Ajayan, *Cell Rep. Phys. Sci.*, 2024, **5**, 101851.
17 S. D. Magar, C. Leibing, J. L. Gómez-Urbano, D. Carriazo and A. Balducci, *Energy Technol.*, 2022, **10**, 2200379.
18 S. D. Magar, C. Leibing, J. L. Gómez-Urbano, R. Cid, D. Carriazo and A. Balducci, *Electrochim. Acta*, 2023, **446**, 142104.
19 A. Bagreev, F. Adib and T. J. Bandosz, *Carbon*, 2001, **39**, 1897–1905.
20 M. Olszewski, P. Arauzo, M. Wądrzyk and A. Kruse, *J. Anal. Appl. Pyrolysis*, 2019, **140**, 255–263.
21 K. MacDermid-Watts, E. Adewakun, T. D. Abhi, R. Pradhan and A. Dutta, *J. Environ. Chem. Eng.*, 2021, **9**, 105431.
22 J. L. Gómez-Urbano, G. Moreno-Fernández, M. Arnaiz, J. Ajuria, T. Rojo and D. Carriazo, *Carbon*, 2020, **162**, 273–282.
23 X. Sun, X. Zhang, W. Liu, K. Wang, C. Li, Z. Li and Y. Ma, *Electrochim. Acta*, 2017, **235**, 158–166.
24 A. C. Ferrari and J. Robertson, *Phys. Rev. B: Condens. Matter Mater. Phys.*, 2000, **61**, 14095.
25 A. Merlen, J. G. Buijnsters and C. Pardanaud, *Coatings*, 2017, **7**, 153.
26 A. C. Ferrari, *Solid State Commun.*, 2007, **143**, 47–57.
27 R. Yuan, Y. Guo, I. Gurgan, N. Siddique, Y.-S. Li, S. Jang, G. A. Noh and S. H. Kim, *Carbon*, 2025, 120214.
28 J.-B. Wu, M.-L. Lin, X. Cong, H.-N. Liu and P.-H. Tan, *Chem. Soc. Rev.*, 2018, **47**, 1822–1873.
29 F. Adar and P. Miao, *Spectroscopy*, 2025, **40**, 6–11.
30 A. Sadezky, H. Muckenhuber, H. Grothe, R. Niessner and U. Pöschl, *Carbon*, 2005, **43**, 1731–1742.
31 H. D. Asfaw, R. Gond, A. Kotronia, C.-W. Tai and R. Younesi, *Sustainable Mater. Technol.*, 2022, **32**, e00407.
32 Z. Xing, Y. Qi, Z. Tian, J. Xu, Y. Yuan, C. Bommier, J. Lu, W. Tong, D.-E. Jiang and X. Ji, *Chem. Mater.*, 2017, **29**, 7288–7295.
33 A. Cuesta, P. Dhamelincourt, J. Laureyns, A. Martínez-Alonso and J. D. Tascón, *Carbon*, 1994, **32**, 1523–1532.
34 D. G. Henry, I. Jarvis, G. Gillmore and M. Stephenson, *Earth-Sci. Rev.*, 2019, **198**, 102936.
35 Z. Li, C. Lu, Z. Xia, Y. Zhou and Z. Luo, *Carbon*, 2007, **45**, 1686–1695.
36 A. Beda, F. Rabuel, M. Morcrette, S. Knopf, P.-L. Taberna, P. Simon and C. M. Ghimbeu, *J. Mater. Chem. A*, 2021, **9**, 1743–1758.
37 R. E. Franklin, *Acta Crystallogr.*, 1951, **4**, 253–261.
38 H. P. Klug and L. E. Alexander, *X-ray Diffraction Procedures: for Polycrystalline and Amorphous Materials*, 1974.
39 H. D. Asfaw, C.-W. Tai, M. Valvo and R. Younesi, *Mater. Today Energy*, 2020, **18**, 100505.
40 J. Ø. Halvorsen, P. Stacey, P. Graff, E. L. Folven Gjengedal and T. K. Ervik, *J. Occup. Environ. Hyg.*, 2025, **22**, 248–258.
41 T. R. Kumar, R. A. Senthil, Z. Pan, J. Pan and Y. Sun, *J. Energy Storage*, 2020, **32**, 101903.
42 H. Liu, H. Liu, S. Di, B. Zhai, L. Li and S. Wang, *ACS Appl. Energy Mater.*, 2021, **4**, 4955–4965.
43 R. Tian, S.-H. Park, P. J. King, G. Cunningham, J. Coelho, V. Nicolosi and J. N. Coleman, *Nat. Commun.*, 2019, **10**, 1933.
44 X. Dai, S. Lei, J. Liu, Z. Shang, S. Zhong and X. Li, *J. Power Sources*, 2021, **498**, 229912.
45 T. Panja, J. Ajuria, N. Díez, D. Bhattacharjya, E. Goikolea and D. Carriazo, *Sci. Rep.*, 2020, **10**, 10842.
46 G. Dobele, A. Volperts, A. Plavniece, A. Zhurinsh, D. Upskuviene, A. Balciunaite, G. Niaura, L. C. Colmenares-Rausseo, L. Tamasauskaite-Tamasiunaite and E. Norkus, *Molecules*, 2024, **29**, 2238.
47 F. Tuinstra and J. L. Koenig, *J. Chem. Phys.*, 1970, **53**, 1126–1130.
48 X.-Y. Zhao, J.-P. Cao, K. Morishita, J.-I. Ozaki and T. Takarada, *Energy Fuels*, 2010, **24**, 1889–1893.
49 D. Lozano-Castello, D. Cazorla-Amorós, A. Linares-Solano, S. Shiraishi, H. Kurihara and A. Oya, *Carbon*, 2003, **41**, 1765–1775.
50 J. Wang and S. Kaskel, *J. Mater. Chem.*, 2012, **22**, 23710–23725.
51 C. H. Kwak, D. Kim and B. C. Bai, *Molecules*, 2022, **27**, 1454.
52 R. Mendoza, J. Oliva and V. Rodriguez-Gonzalez, *Int. J. Energy Res.*, 2022, **46**, 6989–7020.
53 B. Xu, F. Wu, R. Chen, G. Cao, S. Chen, Z. Zhou and Y. Yang, *Electrochem. Commun.*, 2008, **10**, 795–797.
54 M. Dotoli, E. Milo, M. Giuliano, R. Rocca, C. Nervi, M. Baricco, M. Ercole and M. F. Sgroi, *Batteries*, 2021, **7**, 46.

55 X. Sun, Y. An, X. Zhang, K. Wang, C. Yuan, X. Zhang, C. Li, Y. Xu and Y. Ma, *Batteries*, 2022, **9**, 11.
56 O. E. Eleri, F. Huld, J. Pires, W. M. Tucho, P. Schweigart, A. M. Svensson, F. Lou and Z. Yu, *Electrochim. Acta*, 2023, **453**, 142359.
57 S. S. Zhang, *J. Solid State Electrochem.*, 2017, **21**, 2029–2036.
58 O. E. Eleri, J. Pires, F. T. Huld, S. Lu, P. Schweigart, A. M. Svensson, F. Lou and Z. Yu, *Sustainable Energy Fuels*, 2023, **7**, 1846–1854.
59 N. El Ghossein, A. Sari, P. Venet, S. Genies and P. Azaïs, *J. Energy Storage*, 2021, **33**, 102039.
60 M. Schroeder, M. Winter, S. Passerini and A. Balducci, *J. Power Sources*, 2013, **238**, 388–394.
61 B. Babu, P. Simon and A. Balducci, *Adv. Energy Mater.*, 2020, **10**, 2001128.
62 L. Caizán-Juanarena, M. Arnaiz, E. Gucciardi, L. Oca, E. Bekaert, I. Gandiaga and J. Ajuria, *Adv. Energy Mater.*, 2021, **11**, 2100912.